Osteoinductively functionalized 3D-printed scaffold for vertical bone augmentation in beagle dogs

Wang, T.; Xu, G.L.; Zhang, C.K.; Forouzanfar, T.; Liang, J.W.; Pan, Y.L.; ... ; Lin, H.Y.

Clinical Implant Dentistry and Related Research

WILEY

ORIGINAL ARTICLE

Osteoinductively Functionalized 3D-Printed Scaffold for Vertical Bone Augmentation in Beagle Dogs

Ting Wang[1] | Gaoli Xu[2] | Chuankai Zhang[3] | Tymour Forouzanfar[1] | Junwei Liang[4] | Yulei Pan[5] | Chenxi Shen[1,6] | Gang Wu[3] | Haiyan Lin[3,7]

[1]Department of Oral and Maxillofacial Surgery, Leiden University Medical Center (LUMC), Leiden, The Netherlands | [2]School/Hospital of Stomatology, Zhejiang Chinese Medical University, Hangzhou, China | [3]Savid School of Stomatology, Hangzhou Medical College, Hangzhou, China | [4]Department of Stomatology, Zhejiang Chinese Medical University, Hangzhou, China | [5]The Second Affiliated Hospital of Zhejiang University School of Medicine, Hangzhou, China | [6]Hangzhou Huibo Science and Technology Co. Ltd., Hangzhou, China | [7]Department of Implantology, Hangzhou Stomatology Hospital, Hangzhou, China

Correspondence: Gang Wu (gwu@dencosparo.nl) | Haiyan Lin (lhaiyanlily@163.com)

Received: 9 June 2024 | **Revised:** 15 September 2024 | **Accepted:** 6 October 2024

Funding: This work was supported by China Scholarship Council (Grant No. 202308330121) and Key Research and Development Program of Zhejiang Province (Grant No. 2023C03070 and 2021C04013).

Keywords: 3D printed scaffold | biomimetic | bone morphogenetic protein-2 | hyaluronic acid | nanocrystalline calcium phosphate | vertical bone regeneration

ABSTRACT

Objective: To evaluate the efficacy of 3D-printed scaffolds that were osteoinductively functionalized with a bone morphogenetic protein 2 (BMP-2)-incorporated biomimetic calcium phosphate particles (BMP-2-inc. BpNcCaP)/hyaluronic acid (HA) composite gel in vertical bone augmentation in beagle dogs.

Materials and Methods: Four Beagle dogs were used in this study. Three months after the extraction of 1st, 2nd, 3rd, and 4th premolars at both sides of the lower jaws of Beagle dogs, one or two critical-size vertical bone defects (4 mm vertical bone defect without buccal and lingual bone) on each side were surgically created. The defects were randomly subjected to the following groups: (1) Control (without bone-defect-filling materials); (2) 3D scaffold; (3) BMP2-inc. BpNcCaP/HA-functionalized 3D scaffold. Six weeks post-surgery, samples were harvested and subjected to micro-CT and histomorphometric analyses.

Results: The struts of the BMP2-inc. BpNcCaP/HA-func. 3D scaffold were covered by a thick layer of cemented irregular particles with an average pore size at $327 \pm 27\,\mu m$. The BpNcCaP/HA-func. 3D scaffold group bore significantly higher bone volume, bone volume fraction, trabecular number, trabecular thickness, bone mineral density, connectivity density, and bone volumes in three directions (mesiodistal, buccolingual, and apicocoronal) when compared with the groups of Control and 3D scaffold. Moreover, the BMP2-inc. BpNcCaP/HA-func. 3D scaffold group bore significantly lower trabecular separation and exhibited significantly higher bone-to-scaffold contact percentage and newly formed bone area percentage within pores in comparison with 3D scaffold.

Conclusions: BMP2-inc. BpNcCaP/HA-func. 3D scaffold dramatically enhanced vertical alveolar bone augmentation, which suggests a promising application potential of BMP2-inc. BpNcCaP/HA-func. 3D scaffold in dental clinic.

1 | Introduction

Severe alveolar ridge bone resorption may occur after tooth extraction particularly in the cases with thin bone wall, trauma, or periodontitis, which causes severe insufficiency of horizontal and vertical bone volume in further implantation treatment [1–3]. Hitherto, various clinical techniques have been developed to facilitate horizontal ridge augmentation with predictable outcome [4–6]. In contrast, vertical bone augmentation still remains highly challenging due to the difficulties in providing a mechanically stable scaffold and adequate regenerative elements to support sufficient new bone formation [7, 8]. Monocortical autograft is an effective treatment for vertical bone augmentation because it contains osteoconductive scaffolds, osteoinductive growth factors, and osteogenic cells [9, 10]. However, its application is also associated with a series of drawbacks, such as the need for a second surgery, donor-site pain and morbidity, limited availability, fast resorption rate and difficulty in intraoperative shaping [11]. Particulated allogeneic and xenogeneic bone grafts are less favorable alternatives as they need skill-sensitive interventions (e.g., titanium mesh and non-resorbable membrane) to obtain desirable three-dimensional (3D) geometry and mechanical stability [12]. As a promising option, 3D printing technology enables the production of patient-personalized and anatomically matched 3D scaffolds and constructs with high tunability in porosity and pore size. Various 3D printing techniques, such as material extrusion and powder bed fusion, have been developed to print calcium phosphate (CaP)-based bone scaffolds [13]. To facilitate rapid bone regeneration for vertical bone augmentation, 3D printed scaffolds still need to be conferred osteogenic elements.

One common method to confer osteogenic elements in clinic is to apply bone morphogenetic protein-2 (BMP-2). BMP-2 is a growth factor from the superfamily of transforming growth factor-β (TGF-β) and bears potent osteoinductivity [14]. Medical devices containing absorbable collagen sponge (Medtronic) or CaP cement (CPC Powder, Rebone, Shanghai) and BMP-2 are adopted for a series of orthopedic applications, such as spine fusion, open fracture, anterior interbody fusion, and posterolateral lumbar fusion [15]. However, in all the clinically available medical devices, BMP-2 is superficially adsorbed onto the carrier materials, which may yield burst release and thus a series of side effects, such as osteolysis due to over-stimulated osteoclastic activity and bone formation in unintended sites [16].

In our previous study [17], we successfully developed a novel type of CaP particles—biomimetically-precipitated nanocrystalline CaP (BMP2-inc. BpNcCaP), which can internally incorporate and slowly release BMP-2. Furthermore, we also showed that hyaluronic acid gel (HA) may promote the osteogenic and angiogenic activities induced by BMP2 [48]. In this study, we aimed to apply the BMP2-inc. BpNcCaP/HA to functionalize 3D printed scaffolds so as to promote vertical bone augmentation. For this purpose, we adjusted the formulations of BMP2-inc. BpNcCaP/HA by manipulating the size of BMP2-inc. BpNcCaP particles and the concentration of HA so that BMP2-inc. BpNcCaP/HA could penetrate into the pores of 3D printed scaffolds and form a homogenous and thick layer of coating on the struts of the scaffolds. Using a vertical jaw bone defect model in beagle dogs, we evaluated the efficacy of 3D printed CaP scaffolds functionalized with BMP2-inc. BpNcCaP/HA (BMP2-inc. BpNcCaP/HA-func. 3D scaffold) in vertical bone augmentation.

2 | Materials and Methods

2.1 | Study Design

The animal study was approved by the Ethical Committee of Zhejiang Chinese Medical University (No. IACUC-202401-03). We evaluated the efficacy of BMP2-inc. BpNcCaP/HA-func. 3D scaffolds in vertical bone augmentation. For this purpose, we surgically created two-wall critical-size bone defects on alveolar bones in beagle dogs. Critical-size defects (CSD) originally referred to the smallest defects that would not heal by natural process during the life-time of the animal [18–21]. Because the animal lifetime in most of clinical research is bounded by the completion of the studies, the CSD concept was revisited recently to refer to the smallest size of a defect that does not heal spontaneously when left untreated for a certain period [19]. A recent review concluded that there was a lack of homogeneity in reporting data on CSDs in the dog mandible [22]. In our animal study, the bone defect in the Control group did not heal within the monitoring span. Therefore, according to the above-mentioned definition of CSD, the defects in our study might be considered as a CSD of Beagle dogs.

Three groups and four samples per groups were set up. In previous studies on vertical alveolar bone augmentation in beagle dogs [23–25], the set of sample size at 4–6 animals per group was adopted. Therefore, in this study, we first set the sample size at four and thereafter we used the achieved data to conduct a power analysis in order to check the adequacy of the sample size. The power analysis result using the achieved data from this study confirmed adequacy of the sample size in our study. Four male beagle dogs (12-month-old, 15–17 kg in weight) were used in this randomized study and treated following the ARRIVE guidelines for preclinical animal studies (Table S1). Before the experiment, there was one-week period to standardize feeding and environment factors on all dogs. The dogs were housed individually in kennels with free access to water and feed according to the general feeding program at the Experimental Animal Center of State Key Laboratory of Biotherapy. The whole extraction and vertical bone augmentation surgery were performed by the same surgeon with a 5-year clinical experience.

2.2 | Preparation of the 3D Scaffolds

3D scaffolds (Figure 1C) that were fabricated via digital light processing with three-dimensional sizes of 5 mm × 8 mm × 5 mm (W × L × H) were purchased from TEN DIMENSIONS, China. The scaffolds consisted of 80 wt% TCP and 20 wt% HAp and bore rectangular parallelepiped structure (Figure 1A). The strut diameter was about 400 μm (d1) and the distance between adjacent struts was about 800 μm (d2) (Figure 1B). During the printing of the scaffolds, a channel was reserved in the center of each scaffold for fixation with titanium screw. The size of the upper part of the channel was 1.8 mm (H1) in length and 2.7 mm (φ1) in diameter, and the size of the lower part was 3.2 mm (H2) in length channel is 1.6 mm (φ2) in diameter (Figure 1B).

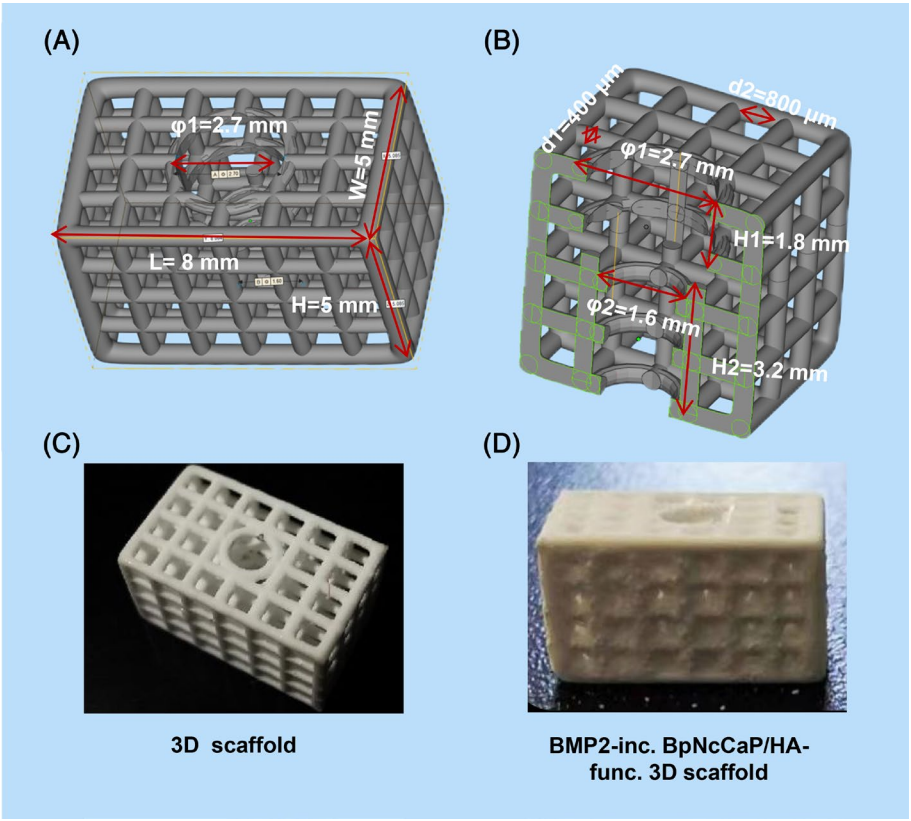

FIGURE 1 | (A, B) Schematic diagram of Digital light processing (DLP)-based 3D printing for the preparation of porous CaP ceramics with three dimensional sizes of 5 mm × 8 mm × 5 mm (W × L × H). Figure showing that the strut diameter was about 400 μm (d1), the distance between adjacent struts was about 800 μm (d2), the size of the upper part of the channel was 1.8 mm (H1) in length and 2.7 mm (φ1) in diameter, and the size of the lower part was 3.2 mm (H2) in length channel is 1.6 mm (φ2) in diameter. (C) 3D-printed calcium phosphate scaffold (3D scaffold) were fabricated via digital light processing. (D) 3D scaffold functionalized with a bone morphogenetic protein-2-biomimetic calcium phosphate particles/hyaluronic acid composite gel (BMP2-inc. BpNcCaP/HA) to form BMP2-inc. BpNcCaP/HA-func. 3D scaffold.

2.3 | Preparation of the BMP2-Inc. BpNcCaP/HA-Func. 3D Scaffolds

BMP2-inc. BpNcCaP granules (50 μg BMP-2/0.08 g BpNcCaP) were made according to our previously published protocol [17]. The granules were further ground into powders and sieved with 150 μm-diameter filters to achieve the powers with their diameters less than 150 μm. Mix the 1000 μg BMP2-inc. BpNcCaP powders in the 1.5 mL HA gel (1600 KDa, 5 mg/mL) at room temperature and vortex to form a stable suspension of BMP2-inc. BpNcCaP/HA. Thereafter, drop 410 μL of BMP2-inc. BpNcCaP/HA suspension onto a scaffold and let the suspension flow along the struts into the scaffold. Turn the scaffolds carefully so as to form a homogenous distribution of the suspension on and within the 3D scaffolds. The final loadings of BMP-2, BpNcCaP and HA per scaffold were 64 μg, 102 μg and 1.2 mg, respectively. The BMP2-inc. BpNcCaP/HA-func. 3D scaffolds were then dried in safety cabinet overnight for subsequent experiments (Figure 1D). The entire procedure was conducted under sterile conditions.

2.4 | Microstructure and Pore Size Analysis

The microstructures of 3D scaffolds and BMP2-inc. BpNcCaP/HA-func. 3D scaffolds were examined by scanning electron microscopy (SEM, S3400N, Hitachi, Japan). Before observation, the specimens were dried at room temperature and sputter-coated with Au plasma. Four samples of 3D scaffolds and BMP2-inc. BpNcCaP/HA-func. 3D scaffolds were measured under SEM to assess their average pore diameters.

2.5 | In Vivo Experiments

Pre-molar area in mandible was selected to create the vertical bone augmentation model. In comparison with the anterior teeth area and posterior molar area, the pre-molar area has been more commonly adopted in previous studies to create critical size bone defects for vertical bone augmentations in jaw bone [25–27]. This selection is mainly attributed to sufficient mouth opening, mesial-distal distance and RBH (the alveolar crest to the mandibular canal) as well as minimal bone inclination and teeth extraction difficulty. Minimally invasive extraction techniques were applied to extract the 1st–4th premolars at both lower jaws of Beagle dogs. The extraction surgery was performed under general and local anesthesia. The general anesthesia was induced by intravenous Propofol Injection (5.5 mg/kg) accompanied by penicillin (5×10^4 U/kg) and atropine (0.05 mg/kg). During general anesthesia, tracheal intubation was performed to maintain an open airway. Multi-Parameter Monitor (SurgiVet V9204, USA) was used to

monitor the electrocardiogram, heart rate, respiratory rate, oxygen saturation, temperature, blood pressure. Local anesthesia was performed with the local injection of 1% lidocaine containing adrenaline at a concentration of 1:100000. Skin disinfection with 0.5% iodophor solution was done at the surgery site. The wound was then disinfected with 10% povidone-iodine. After surgery, the dogs received anti-inflammatory and analgesic drugs for 7 days.

Three months after tooth extraction, anesthesia and poster-surgery care were performed as above described to facilitate the vertical bone augmentation experiments. There were four potential implantation sites in one animal (e.g., mesial site on left mandible, distal site on left mandible, mesial site on right mandible and distal site on right mandible) and there were 16 potential implantation sites in four animals. We set up three groups: (1) no bone-defect-filling materials (Control group); (2) filled with unfunctionalized 3D scaffold as negative control (3D scaffold group); (3) filled with BMP2-inc. BpNcCaP/HA-func. 3D scaffold as experimental group (BMP2-inc. BpNcCaP/HA-func. 3D scaffold group). To balance the potential influence of different implantation sites (mesial/distal and left/right) on the efficacy of vertical bone augmentation, four distribution patterns (Figure S1) were designed to guarantee that four samples in one group were distributed in the four sites respectively. The four distribution patterns were randomly assigned to the four dogs. Finally, three implantation sites were created in each dog.

After an incision between the mandibular canines and the 1st molars, buccal and lingual mucoperiosteal flaps were lifted to expose the underlying bone tissue. One or two CSD [18–20, 28] with 4 mm vertical bone loss, 10 mm in mesiodistal length, and without buccal and lingual bone (W × L × H: 5 mm × 10 mm × 4 mm) on each side of jaw bone were surgically created using a high-speed turbine (Figure 2A–C). 3D scaffolds were fixed onto the alveolar ridge by titanium screws (Figure 2D). The interval between two defects was set at 1 cm so as to prevent the translocation of BMP-2. Finally, the buccal and lingual mucoperiosteal flaps were sutured without any tension (Figure 2E). Particularly, the distal margin of the mesial site and the mesial margin of the distal site were respectively tightly sutured, thereby preventing potential diffusion of BMP-2. The wounds were then disinfected with 10 povidone-iodine. Thereafter, the implantation sites were evaluated using 16-slice head Multi-Slice Computed Tomography (MSCT) and periapical films. After surgery, the dogs received anti-inflammatory and analgesic drugs for 7 days.

Six weeks after the surgery, all dogs were sacrificed using an overdose of anesthesia thiopental (Sumianxin II). This observation time point was selected in order to observe the promoting and accelerating effect of BMP2-inc. BpNcCaP/HA-func. 3D scaffold on the vertical augmentation of alveolar bone. The bone-defect-filling materials were retrieved together with the surrounding tissues from the mandibles and immediately fixed in 4% paraformaldehyde solution for 2 days.

2.6 | Micro-Computed Tomography (Micro-CT)

In total, 12 bone sample blocks were scanned with a high-resolution micro-CT (μCT 100, Scanco Medical AG,

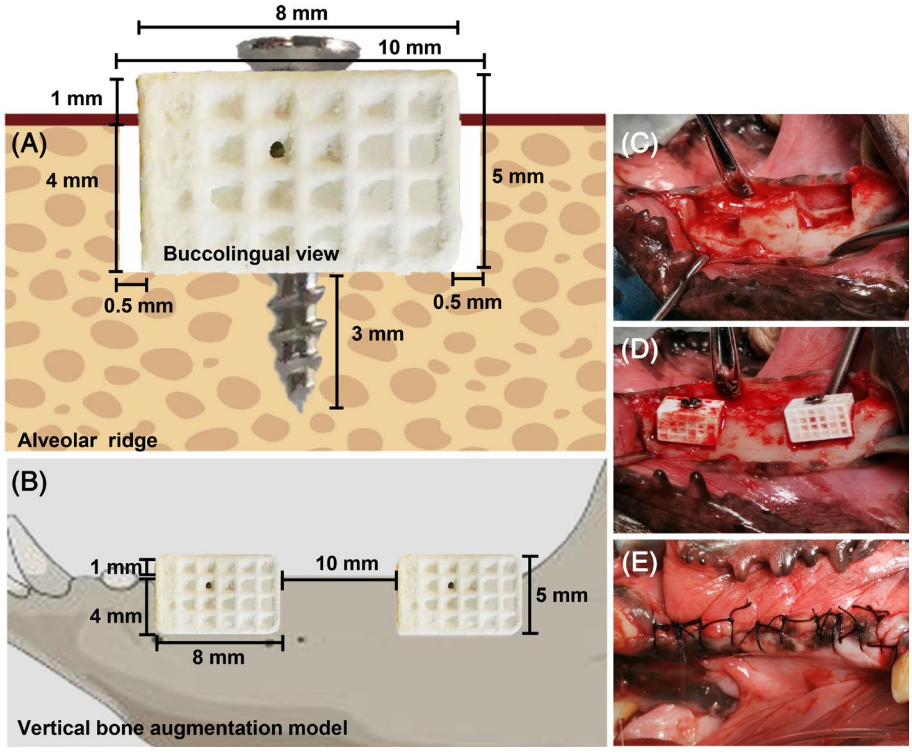

FIGURE 2 | (A, B) Buccolingual view of the design of vertical bone augmentation model in beagle dogs. The critical-size vertical bone defects with 4 mm vertical bone loss, 10 mm in mesiodistal length, and without buccal and lingual bone (W × L × H: 5 mm × 10 mm × 4 mm) on each side of jaw bone. (C) One or two critical-size vertical bone defects on each side of Beagle dog mandible jaw bone were surgically created. (D) The 3D scaffolds and BMP2-inc. BpNcCaP/HA-func. 3D scaffolds were fixed onto the alveolar ridge by titanium screws. (E) Tension-free suturing of mucoperiosteal flaps.

Switzerland). The x-ray source was operated at a voltage of 100 kVP and current of 200 μA with an exposure time of 300 ms, at a resolution of 30 μm (70 kVP, 200 μA, 30 μm, 300 ms) and then subjected to offline reconstruction. The reconstructed images were 906 × 906 pixels with the pixel size of 30 μm. Beam hardening artifact was corrected during reconstruction by the reconstruction software. The CT analyzer software (Bruker Micro-CT NV, Kontich, Belgium) was used to define a region of interests (ROIs) on the two-dimensional images to obtain a volume of interests (VOIs) dataset. The selected VOI was a cuboid with 5 mm in buccolingual width, 10 mm in mesiodistal length, 5 mm in apicocoronal height (W × L × H: 5 mm × 10 mm × 5 mm) (Figure 5A). Three-dimensional reconstruction was performed using CT analyzer and viewed by Materialise's interactive medical image control system (MIMICS, Materialise).

Since the quantity of newly formed bone could vary along the distance from original bone to the bone graft material. The VOI was also analyzed in three directions: mesiodistal, buccolingual and apicocoronal, respectively (Figure 6A). The VOI was divided into trisection in mesiodistal direction (Figure 6A1), the mesial volume (VOI-mesial), the middle volume (VOI-middle), and the distal volume (VOI-distal). The VOI was divided into trisection in buccolingual direction (Figure 6A2), the buccal volume (VOI-buccal), the middle volume (VOI-middle), and the lingual volume (VOI-lingual). The VOI was divided into trisection in apicocoronal direction (Figure 6A3), the coronal volume (VOI-coronal), the middle volume (VOI-middle), and the apical volume (VOI-apical). All the images were binarized using the same grayscale thresholds (newly formed bone: 220–500; 3D scaffold: 600; titanium screw: 600).

We evaluated the micro-architectures of bone using the following parameters: (1) bone volume (BV); (2) bone volume/tissue volume (BV/TV); (3) trabecular separation (Tb.sp., mm); (4) trabecular number (Tb.N, 1/mm); (5) trabecular thickness (Tb.Th, mm); (6) bone mineral density (BMD; mg HA/cm^3); and (7) connectivity density (Conn.D, 1/mm^3). For the measurement of above observation indicators, the number of bone pixels in the VOI divided by the total number of pixels in the VOI was used to.

2.7 | Histology Procedures

After micro-CT analysis, the samples were rinsed with running water for 24 h. Then, they were dehydrated in ascending degrees of ethanol and embedded in methylmethacrylate (MMA, Technovit 7200; Heraeus Kulzer). Samples were cut using a Leica diamond saw fitted in a Leica SP1600 slicing machine (Leica Microsystems, Wetzlar, Germany). One sample was cut into 10–12 slices, 600 μm in thickness and 1 mm apart. The slices were mounted on plexiglas holders, polished, and surface-stained with McNeal's tetrachrome, basic fuchsine and toluidine blue [29]. Using this protocol, newly-formed bone stains deep red, cell nuclei blue, collagen fibers pink and the scaffold pale red. The slices were then examined in a Nikon-Eclipse E-1000 light microscope and photographed in color at a different magnification of 20, 40, 100, and 200. Approximately nine photomicrographs were collected per sample. These prints were used for the histomorphometric analysis of the various stereological estimators. The same VOI-mesial, VOI-middle, and VOI-distal from the micro-CT analysis were used for the measurements of each parameter.

The bone-to-scaffold contact percentage on the bottom struts and within pores were measured using the Image-Pro Plus (IPP, MEDIA CYBERNETICS). The bone percentage within pores were measured by the point-counting technique [30].

For each histological slice, the length of new bone contact on the bottom struts of scaffolds (Lnbs, μm) and the whole length of the bottom struts of scaffolds (Ls, μm) within area of interest (AOI) were measured using the Image-Pro Plus. The bone-to-scaffold contact percentage on the bottom struts (% BSCs) was calculated using the following formula:

$$\%\,\mathrm{BSCs} = (\mathrm{Lnbs}, \mu\mathrm{m}) / (\mathrm{Ls}, \mu\mathrm{m}) \times 100\,\%$$

For each histological slice, the length of new bone contact within pores of scaffolds (Lnbp, μm) and the whole length of the pores surface of 3D scaffolds (Lw, μm) within area of interest (AOI) were measured using the Image-Pro Plus. The bone-to-scaffold contact percentage within pores (% BSCp) was calculated using the following formula:

$$\%\,\mathrm{BSCp} = (\mathrm{Lnbp}, \mu\mathrm{m}) / (\mathrm{Lw}, \mu\mathrm{m}) \times 100\,\%$$

For each histological slice, the surface area of newly formed bone within pores (Snb) and the whole area of the pores within VOI-mesial, VOI-middle, and VOI-distal (Sv) were measured using the point-counting technique [30]. The interval between two slices was 1 mm. The tissue volume within the selected region can be estimated as the sum of the cross-sectional areas multiplied by the 1-mm interval from all the selected slices. The newly formed bone percentage (%NB) within pores was calculated using the following formula:

$$\%\,\mathrm{NB} = [(\Sigma\,\mathrm{Snb}) \times 1\ \mathrm{mm}] / [(\Sigma\,\mathrm{Sv}) \times 1\ \mathrm{mm}] \times 100\,\%$$

2.8 | Statistical Analysis

The person who conducted all the measurements was blinded to the group set up. All data were presented as mean ± standard deviation (mean ± SD). Data were compared using one-way analysis of variance (ANOVA), and Bonferroni's correction was used for post hoc comparison. Statistical analysis was performed in SPSS 25.0 (IBM Information Management). A value of $p < 0.05$ was considered to be statistically significant.

3 | Results

All animals recovered well and all the implantation sites healed uneventfully during the experimental period. Immediate postoperative MSCT imaging showed that all the bone graft materials were stably implanted and have normal three-dimensional spatial position (Figure 3A). During the observation period of 6 weeks after operation, soft tissue surrounding all the bone graft materials was free of any signs of inflammation, such as redness or swelling (Figure 3B). Periapical films showed that all the scaffolds were still located in the desired location and were

complete without significant defect or cracks until euthanasia (Figure 3C).

3.1 | In Vitro Investigation

SEM micrographs showed the geometry and topography of the 3D scaffold (Figure 4A). The 3D scaffolds bore square-shaped and interconnected square macro-pores with an average size at $797 \pm 12\,\mu m$. The struts showed a layered structure with smooth topography on each layer. The average thickness of the struts was about $400\,\mu m$. All the 3D scaffolds had no obvious defects and cracks (Figure 4A1). After the functionalization with BMP-2/BpNcCaP/HA, the struts of the 3D scaffolds were covered by a thick layer of cemented irregular particles (Figure 4B). The average pore size became $327 \pm 27\,\mu m$ (Figure 4B1).

3.2 | Micro-CT Analysis

Six weeks after implantation, the scaffolds and the surrounding tissues were retrieved and subjected to fixation. Thereafter, we adopted micro-CT analysis to quantitatively assess the newly formed bone tissues within and the surrounding the scaffolds (Figure 5A). In the group of Control (no scaffold), there was nearly no significant vertical bone augmentation (Figure 5A1). The 3D scaffolds were only partially penetrated and covered with new bone tissues (Figure 5A2). In contrast, BMP2-inc. BpNcCaP/HA-func. 3D scaffolds were largely covered and penetrated with newly formed bone tissues (Figure 5A3). The total BV in the group of BMP2-inc. BpNcCaP/HA-func. 3D scaffold was $88.21 \pm 6.23\,mm^3$, which was significantly higher than those in the 3D scaffolds group $11.92 \pm 1.17\,mm^3$ and the Control group $2.63 \pm 0.93\,mm^3$. The BV/TV of the newly formed bone in the group of BMP2-inc. BpNcCaP/HA-func. 3D scaffold was 0.35 ± 0.02, which was about 9 and 35 times those in the groups of 3D scaffold (0.04 ± 0.00) and Control (0.01 ± 0.00), respectively (Figure 5B1). Similarly, BMP2-inc. BpNcCaP/HA-func. 3D scaffold group showed the highest mean values in Tb.N (1.82 ± 0.09) 1/mm, Tb.Th ($0.39 \pm 0.06\,mm$), BMD ($904.43 \pm 23.76\,mg\,HA/cm^3$), and Conn.D ($6.55 \pm 0.49$) $1/mm^3$ ($p < 0.05$), which were significantly higher than those in the other two groups (Figure 5B3–B6). BMP2-inc. BpNcCaP/HA-func. 3D scaffold group showed the lowest mean values in trabecular separation (Tb.sp) ($0.188 \pm 0.059\,mm$) among the three groups (3D scaffold group ($0.308 \pm 0.003\,mm$) and Control group ($0.391 \pm 0.025\,mm$)) (Figure 5B2). Except for Tb.Th and Tb.sp., all the parameters in the group of 3D scaffold group were significantly higher than those in the Control group (Figure 5B).

In this animal model, there were original bone tissue in the mesial, distal and apical sites of the scaffolds, while there were no bone tissue in the buccal and lingual sites. This uneven distribution pattern of original bone tissue might cause uneven regeneration of newly formed bone (Figure 6A). To further characterize the distribution pattern of the newly formed bone, we analyzed the BV in three directions: mesiodistal (Figure 6A1), buccolingual (Figure 6A2) and apicocoronal (Figure 6A3). Quantitative analyses showed that in all the three directions, the BVs in the BMP2-inc. BpNcCaP/HA-func. 3D scaffold group were significantly higher than those in the other two groups and the BVs in the 3D scaffold group were also significantly higher than those in the Control group. In all the three groups, the BVs in the mesial and distal 1/3 were similar to each other, which were significantly higher than those in the middle 1/3. The BV in the middle 1/3 of BMP2-inc. BpNcCaP/HA-func. 3D scaffolds was ($21.16 \pm 3.06\,mm^3$), which was about 12 and 23 times those in the groups of 3D scaffolds ($1.60 \pm 0.48\,mm^3$) and Control ($0.89 \pm 0.11\,mm^3$) (Figure 6B1). The similar distribution pattern of newly formed bone was also found in the groups of Control and 3D scaffold in the direction of buccolingual. In contrast, for the group of BMP2-inc. BpNcCaP/HA-func. 3D scaffold, although the BV in the middle 1/3 ($17.97 \pm 1.38\,mm^3$) remained the lowest, the BV in the buccal 1/3 ($44.79 \pm 3.51\,mm^3$) was significantly higher than that in the lingual 1/3 ($29.40 \pm 2.82\,mm^3$) (Figure 6B2). For the Control group, in the direction of apicocoronal, the BV in the apical 1/3 was significantly higher than that in the middle 1/3 and there was no detectable new bone formation in the coronal 1/3. For the group of the 3D scaffold, the BV in the apical 1/3 ($9.96 \pm 0.65\,mm^3$) was about 4 times and 10 times those in the middle 1/3 ($2.61 \pm 0.28\,mm^3$) and coronal 1/3 ($1.10 \pm 0.12\,mm^3$), respectively. In the group of BMP2-inc. BpNcCaP/HA-func. 3D scaffold, BV in the apical 1/3 ($43.71 \pm 1.32\,mm^3$) remained the highest. And there was no significant difference between the latter two 1/3. Furthermore, the difference in BVs between the apical 1/3 and middle/coronal 1/3 was only about 1.7 and 1.6 times, which was much less than that in the groups of 3D scaffold and Control. Furthermore, the volume of newly formed bone in the coronal 1/3 ($27.19 \pm 1.30\,mm^3$) was comparable with that in the middle 1/3 ($24.30 \pm 5.64\,mm^3$) (Figure 6B3).

Furthermore, we also compared the main parameters of the samples in the group of Control or 3D scaffold without adjacent

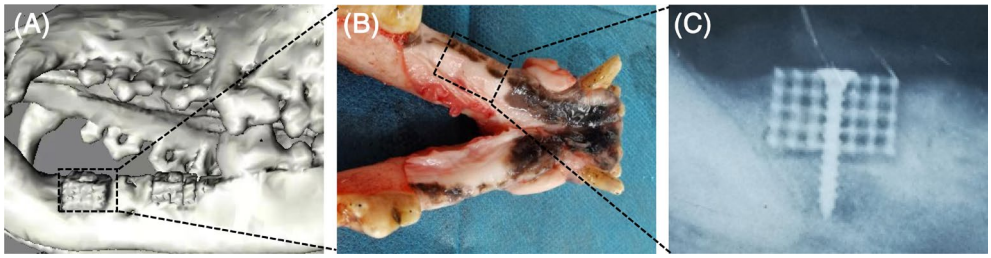

FIGURE 3 | (A) Multi-Slice Computed Tomography (MSCT) image after the vertical bone augmentation in the mandible jaw of Beagle dogs. (B) Gingival healing in the vertical bone augmentation area 6 weeks after the surgery. (C) The periapical films of the vertical bone augmentation area 6 weeks after the surgery.

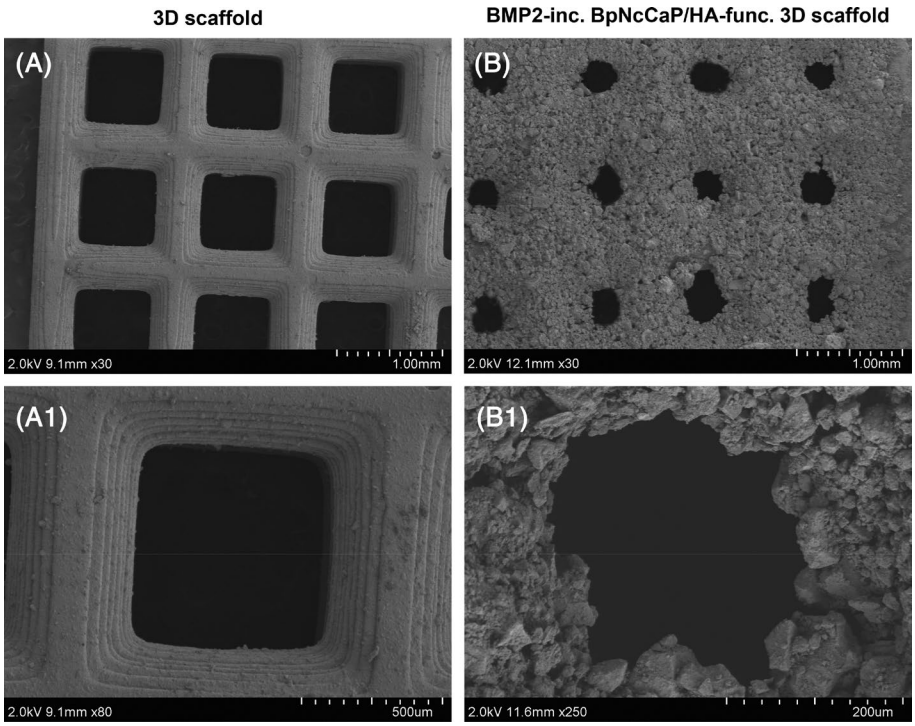

FIGURE 4 | (A) Representative Scanning Electron Microscope (SEM) micrographs showed the geometry and topography of 3D scaffold in a lower magnification (×30). (A1) Higher-magnification (×80) SEM micrographs showing the pore size of 3D scaffold. (B) Representative SEM micrographs of BMP2-inc. BpNcCaP/HA-func. 3D scaffold in a lower magnification (×30), SEM micrographs showing that the struts of the 3D scaffolds were covered by a thick layer of cemented irregular particles. (B1) Higher-magnification (×250) SEM micrographs showing the pore size of BMP2-inc. BpNcCaP/HA-func. 3D scaffold. Scale bar in A and B = 1.00 mm. Scale bar in A1 = 500 μm. Scale bar in B1 = 200 μm.

BMP-2-containing samples with the ones with adjacent BMP-2-containing samples. We found no obvious differences between them, which showed that no significant influence was derived from the adjacent BMP-2-containing samples.

3.3 | Histomorphometric Analysis

Six weeks post-surgery, histological image showed only a thin layer of newly formed bone on the surface of the original bone tissue (Figure 7A1). In the group of 3D scaffold, new bone occurred to the interface between original bone tissue and the scaffolds. Newly formed bone was hardly found within the pores of the 3D scaffolds (Figure 7A2). In contrast, in the group of BMP2-inc. BpNcCaP/HA-func. 3D scaffold, newly formed bone grew into pores and filled the most coronal pores of the scaffolds. Newly formed bone was integrated with the struts of the scaffolds and there are no detectable BMP2-inc. BpNcCaP particles or HA (Figure 7A3). In the 3D scaffold-treated group, the structure of the 3D scaffold was complete, and was surrounded by a little newly formed bone. Most of the newly formed bone was at the bottom and the edge region of the 3D scaffolds, and with less new bone at the coronal part and distributed sporadically in the intra-3D scaffold porosity. On the contrary, it can be seen that the pores of the scaffolds in the BMP-2/BpNcCaP/HA-func. 3D scaffold group were filled with more new bone (NB), and the adhesion area between the new bone and the scaffold was much larger. There were more osteocytes (green arrow) in the new bone and osteoblast on the edge of the scaffold (blue arrow), (Figure 8).

Quantitative analyses showed that the bone-to-scaffold contact percentage on the bottom struts (% BSCs) of BMP2-inc. BpNcCaP/HA-func. 3D scaffolds in the mesial 1/3 was 31.23 ± 1.65%, which was about 6.5 times those of 3D scaffolds (4.85 ± 0.41%). The % BSCs in the middle 1/3 of BMP2-inc. BpNcCaP/HA-func. 3D scaffolds was 27.80 ± 3.83%, which was about 6.2 times those in the group of 3D scaffolds (4.43 ± 1.30%). The % BSCs in the distal 1/3 of BMP2-inc. BpNcCaP/HA-func. 3D scaffolds was 25.56 ± 2.59%, which was about 5.8 times those of 3D scaffolds (4.37 ± 1.29%) (Figure 7B1). There were nearly no new bone within pores of the 3D scaffolds. On the contrary, the newly formed bone percentages within pores (%BV) in the mesial 1/3, in the middle 1/3 and in the distal 1/3 of the BMP2-inc. BpNcCaP/HA-func. 3D scaffolds was 59.63 ± 6.70%, 34.93 ± 4.17%, and 58.82 ± 3.99%, respectively, which were significantly higher than the corresponding values in the 3D scaffolds (Figure 7B2). Similarly, bone-to-scaffold contact percentages within pores (% BSCp) in the mesial 1/3, in the middle 1/3 and in the distal 1/3 of the BMP2-inc. BpNcCaP/HA-func. 3D scaffolds were 43.39 ± 5.21%, 28.26 ± 2.19% and 41.59 ± 5.10%, respectively, which were significantly higher than the corresponding values in the 3D scaffolds (Figure 7B3).

4 | Discussion

Vertical bone augmentation is still highly challenging in the field of dental implantology [1–3]. An ideal bone graft material for vertical bone augmentation should provide precisely matched

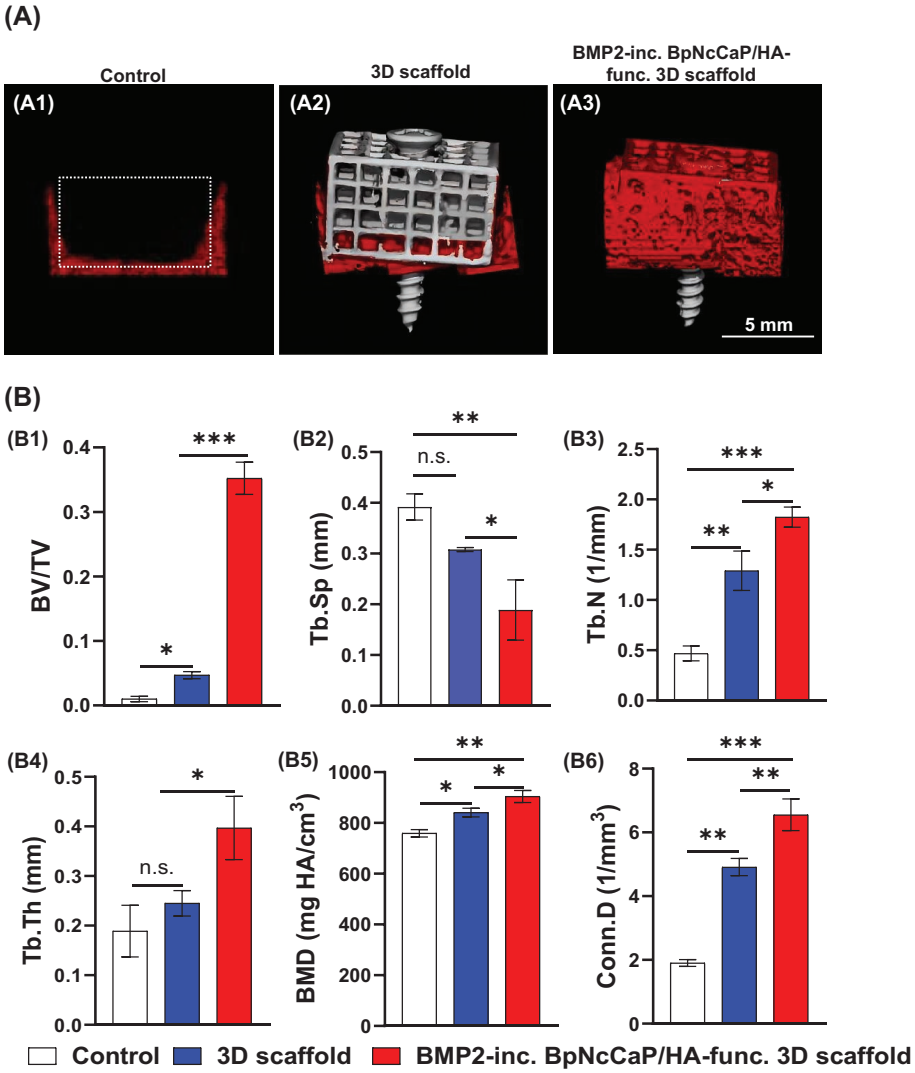

FIGURE 5 | (A) Three-dimensional reconstructed micro-CT images of vertical bone defect sites 6 weeks after the vertical bone augmentation. (White portion: 3D scaffold; Red portion: New bone tissue). (A1) Newly formed bone in VOI of vertical bone defect without bone graft material. (A2) Newly formed bone and grafted biomaterials in VOI of vertical bone defect with 3D scaffold. (A3) Newly formed bone and grafted biomaterials in VOI of vertical bone defect with BMP2-inc. BpNcCaP/HA-func. 3D scaffold. (B) Micro-CT analyses of newly formed bone tissues in VOI of vertical bone defects in the groups of Control, 3D scaffold and BMP2-inc. BpNcCaP/HA-func. 3D scaffolds. (B1) Bone volume/tissue volume (BV/TV). (B2) Trabecular separation (Tb.sp). (B3) Trabecular number (Tb.N), (B4) Trabecular thickness (Tb.Th). (B5) Bone mineral density (BMD). (B6) Connectivity density (Conn.D) (data were presented as mean ± SD, significant effect of the treatment, $*p < 0.05$; $**p < 0.01$; $***p < 0.001$, $n = 4$/group). Scale bar in A1–A3 = 5 mm.

geometry, mechanically stable microenvironment and highly efficient osteoinductivity [31, 32]. Autologous bone block is still a preferable choice for vertical bone augmentation because it not only bears osteoconductive scaffold, osteoinductive growth factors and osteogenic cells but also provides a stable form [33]. However, its wide use is, to some extent, hindered by its limited availability, donor-site pain and morbidity as well as unpredictable resorption rate [34]. As an alternative, a guided bone regeneration (GBR) technique—sausage technique—has been developed and widely adopted in clinic. This technique involves the use of particulate xenograft that bears almost unlimited availability and osteoconductive scaffolds. The production procedure of xenograft always needs sintering at 300-600° so as to remove organic phase and thus maximize biocompatibility, which render it impossible to contain any intrinsic osteoinductive growth factors or osteogenic cells. Therefore, particulate xenograft still needs to be mixed with particulate autologous bone graft to achieve sufficient new bone regeneration, in which the limitation of autologous bone grafts pursues. To achieve bone defect-matching form and stable bone-forming microenvironment, particulate xenograft must be rightly encapsulated by non-resorbable (PTFE) polymeric membrane and titanium pin. Tremendous clinical evidences have shown the success of the sausage technique [35, 36]. However, this technique is also highly clinical skill-sensitive and time-consuming. As an alternative, 3D printed titanium mesh can be adopted to fix xenograft granules [37]. By enabling a pre-design to individually match bone defects, 3D printed titanium mesh is relatively less technique-sensitive. Furthermore, titanium mesh is also more rigid than polymeric membrane to facilitate a stable bone-forming microenvironment [38]. However, the use of titanium mesh is also

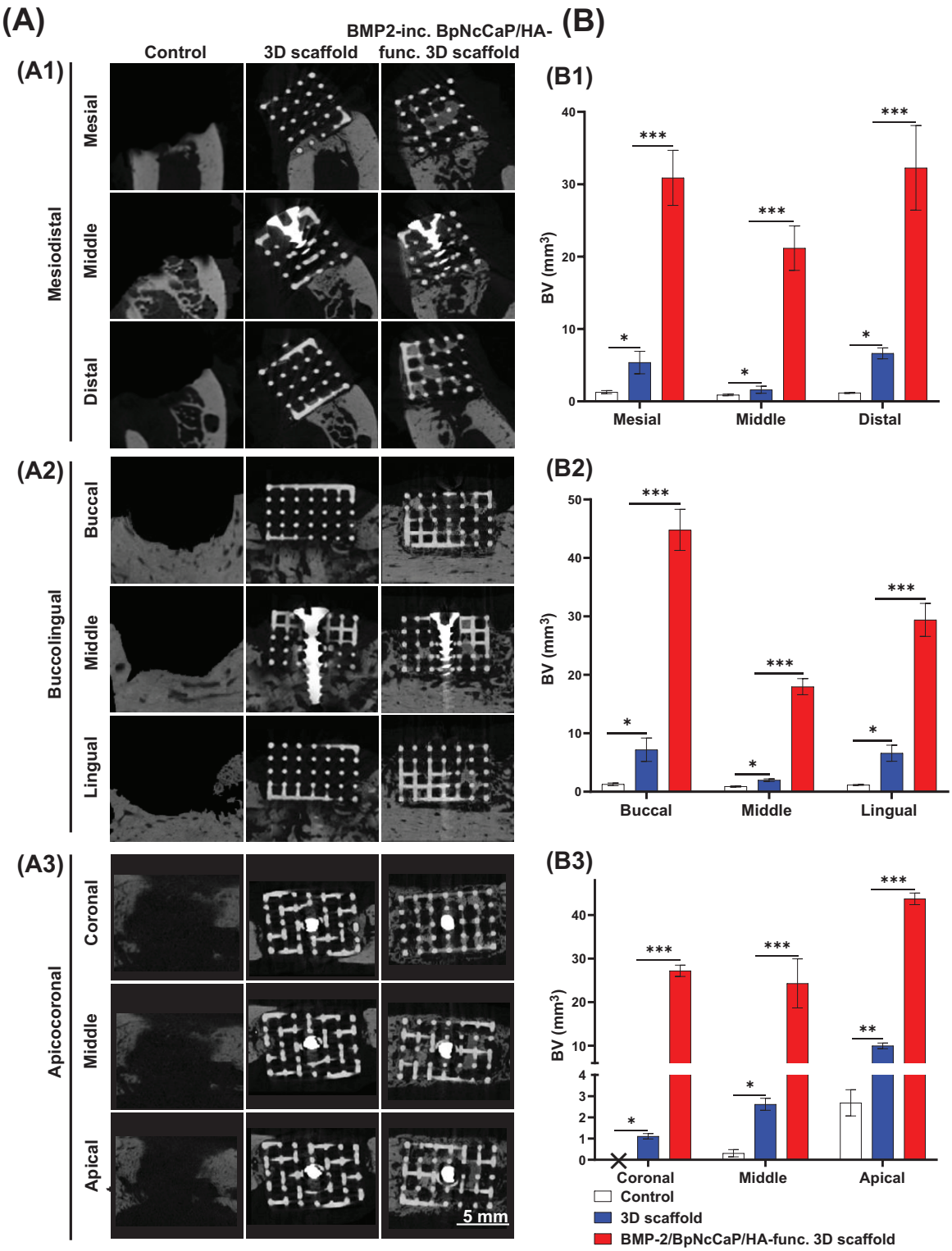

FIGURE 6 | (A) Micro-CT images depicting newly formed bone and grafted biomaterials in three directions 6 weeks after implantation. (A1) The micro-CT images of the three groups were observed in mesiodistal direction. (A2) The micro-CT images of the three groups were observed in buccolingual direction. (A3) The micro-CT images of the three groups were observed in apicocoronal direction. (B) Micro-CT analysis of the bone volume (BV) of the three groups. (B1) Micro-CT analysis of the BV in mesiodistal-VOI of three groups. (B2) Micro-CT analysis of the BV in buccolingual-VOI of three groups. (B3) Micro-CT analysis of the BV in apicocoronal-VOI of three groups (data were presented as mean ± SD, significant effect of the treatment: $^{*}p < 0.05$, $^{**}p < 0.01$, $^{***}p < 0.001$, $n = 4$/group). Scale bar in A = 5 mm.

challenged by potential risk of post-surgery exposure and infection [39]. Therefore, continuous efforts are undertaken to develop next-generation bone graft materials for vertical bone augmentation.

With the rapid development, 3D printing technique may provide a promising solution for vertical augmentation. 3D printing enables the production of patient-personalized and

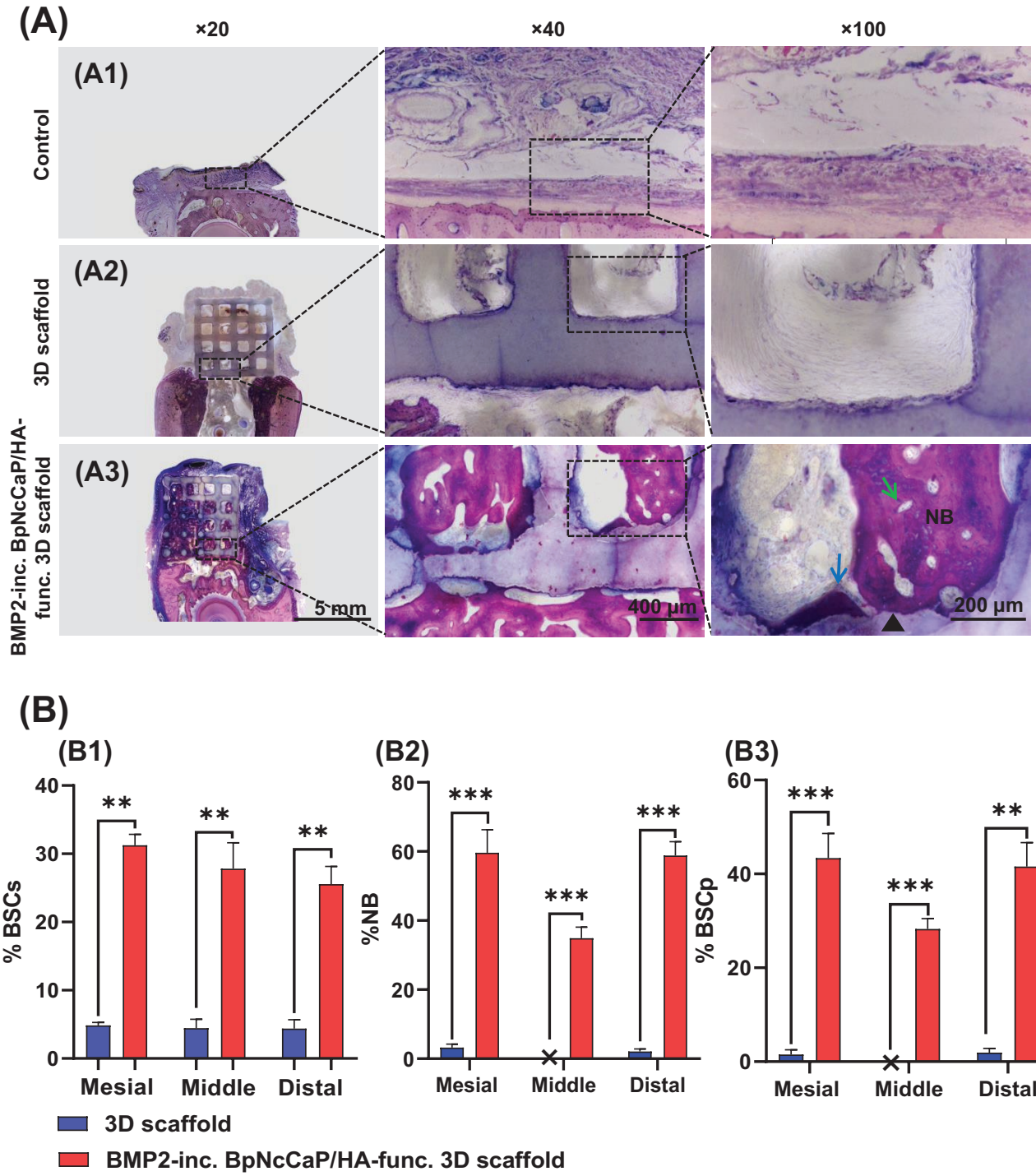

FIGURE 7 | (A) Light micrographs of newly formed bone and grafted biomaterials vertical bone defects 6 weeks after vertical bone augmentation. Light micrographs of three groups in a lower magnification (×20 left column; ×40 middle column; ×100 right column). Bar = 5.0 mm (left column); Bar = 400 μm (middle column); 200 μm (right column). (A1) Light micrographs of the group without bone graft material. (A2) Light micrographs of the group of 3D scaffold. (A3) Light micrographs of the group of BMP2-inc. BpNcCaP/HA-func. 3D scaffold. (B) Light micrographs analysis of three groups. (B1) Light micrographs analysis of the bone-to-scaffold contact percentage on the bottom struts (% BSCs). (B2) Light micrographs analysis of newly formed bone percentage within pores (%NB). (B3) Light micrographs analysis of bone-to-scaffold contact percentage within pores (% BSCp) (data were presented as mean ± SD, significant effect of the treatment: $^{**}p < 0.01$, $^{***}p < 0.001$, $n = 4$/group).

anatomically matched scaffolds [40]. Not only can the outer shape of a scaffold (macroarchitecture) be personalized, but also the microarchitecture, defined as the distribution of the material within the scaffold, can be designed and optimized for bone ingrowth—osteoconduction [41]. However, most of CaP-based 3D printed scaffolds often need a post printing sintering to obtain sufficient mechanical strength and/or remove the organic phase, which makes it nearly impossible to bear intrinsic osteogenic elements [42–44]. As an approach to this problem, BMP-2 may be adsorbed on the 3D scaffolds to

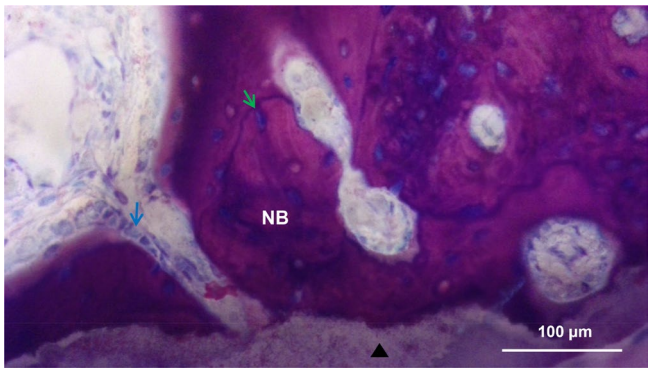

FIGURE 8 | Light micrographs in high magnification (×200) of BMP2-inc. BpNcCaP/HA-func. 3D scaffold that was implanted in mandibular jaw bone defect in beagle dogs for 6 weeks. NB: New bone; Black triangle: Grafted biomaterials; Blue arrow: Osteoblasts; Green arrow: Osteocyte. Scale bar = 100 μm.

confer osteoinductivity. However, after implantation, the superficially adsorbed BMP-2 is usually released in a burst manner, leading to a local, transient and unphysiologically high concentration, which potentially causes a series of side effects, such as swelling and osteolytic bone resorption. Furthermore, the BMP-2 that penetrates into circulation system may also cause ectopic bone induction in unintended area and enhance incidence rate of cancer [45, 46]. Therefore, a slow-release system is highly needed to functionalize 3D printed CaP scaffolds.

In this study, we wished to adopted BMP-2/BpNcCaP particles to osteoinductively functionalize 3D printed CaP scaffolds with a pore size of 800 μm for vertical bone augmentation. For this purpose, we adopted the particles with diameters less than 150 μm so that they may penetrate through and distribute within the pores of the 3D printed CaP scaffolds. In order to facilitate the stickiness of BMP2-inc. BpNcCaP particles on to the struts, we adopted HA gels. The primary reasonability for the adoption of HA gels was that HA is proved to be medical device and thus bears more application potential in clinic than many other materials [47]. Furthermore, after dissolving in PBS, HA may simply form gel with certain viscoelasticity to carry BMP-2/BpNcCaP particles. And more interestingly, we have shown that HA may significantly increase osteogenic and angiogenic activities induced by BMP-2 [48].

The optimal HA molecular weight and concentration was selected to obtain homogenous distribution of BMP-2/BpNcCaP particles within the pores of the 3D printed scaffolds. We found that HA (molecular weight 1600 kDa) with a concentration of 5 mg/mL mixed with BMP-2/BpNcCaP particles could form a stable suspension and also showed sufficient fluidity to flow through the pores of 3D-printed scaffolds. Interconnected porous structure allows nutrient and essential body fluid supply to regenerated cells within the scaffolds for bone tissue engineering. Among the major parameters in designing porous structures, pore size determines the size of the surface support and the density of ligands that can be used for cell adhesion [49–51]. Pore size should be in an appropriate range because too small or too large pore size will either limit nutrient supply, waste removal and cell migration or compromise cell adhesion and scaffold stability [52, 53]. The optimal pore size for bone tissue engineering was initially set between 0.3 and 0.5 mm [54, 55], due to enhanced new bone formation and the formation of capillaries, which is mainly based on the studies on the scaffolds with randomly distributed pores and incorporated BMP-2 in ectopic bone induction models [56]. Another study shows that, for 3D printed scaffolds that bear defined micro-architectures, the pore sizes for optimal osteoconduction (horizontal bone ingrowth) are 0.7–1.2 mm in diameter [57], while pore sizes of 0.5 or 1.5/1.7 mm perform significantly worse (about 33.66% or 31.46% reduction, respectively). Another study evaluates the effects of pore size (0.5, 1.2 and 1.7 mm) of 3D printed scaffolds on osteoconduction (horizontal bone ingrowth) or vertical augmentation (vertical bone ingrowth). It shows that pore size at 1.7 mm is advantageous (about 19.2% enhancement) over pore size at 0.5 mm in vertical augmentation, while no difference was found between pore sizes at 1.2 and 0.5 mm [41]. In clinical practice, most of bone defects may contain more than one condition, such as osteoconduction, vertical augmentation or osteoinduction [58]. In our present study, the vertical bone augmentation model in jaw bone of beagle dogs contains both osteoconduction (horizontal bone ingrowth from distal and mesial direction) and vertical augmentation (bone growth from apical to coronal direction) as well as osteoinduction (due to the presence of BMP-2). Therefore, in order to balance the osteoconduction and vertical augmentation, we selected the 3D printed scaffold with the pore size at 800 μm according the abovementioned studies. And after osteoinductive functionalization, the average pore size was 327 ± 27 μm, which falls in the optimal pore size range (300–500 μm) of the scaffolds with osteoinductive growth factors [55, 59]. Such a design is aiming to maximally facilitate maximal osteoconductive bone ingrowth and regeneration bone induction within the 3D printed scaffolds.

In this study, we adopted a freshly-made bone defect model, which might exhibit a better regenerative potential and less approximation to real clinical situation than pre-existing bone defects. In previous studies [60–62], pre-existing bone defects are more often adopted in relatively smaller defects, such as periodontal bone defects. On the other hand, most of large vertical alveolar bone augmentation models are freshly made, which may be because it is much easier to achieve tension-fresh suturing and uniform defect geometry and thus good comparability among groups. Furthermore, pre-existing bone defects also need a debridement, which, whereas, creates a fresh traumatic bone surface. Six-weeks post-implantation, only very mild new bone formation was detected in the Control group, which indicated that the intrinsic regenerative potential in this model was mild. Furthermore, there was a lack of periosteum-associated new bone formation in all the three groups. Periosteum is shown to an important contributor to new bone regeneration [63]. It provides blood vessels and multipotent stem cells for vascularization and tissue regeneration [64]. In many models, such as calvarial bone defects and periodontal defects, the presence of periosteum significantly promote bone regeneration [24]. On the other hand, previous studies have shown that several microenvironmental conditions, such as mechanical stability, bone-forming space and adjacent bone wall are prerequisite for such an effect of periosteum. Therefore, the absence of periosteum-associated new bone formation might be largely attributed to

mechanical instability and minimal availability of adjacent bone in the large defects in this study.

The parameters of Micro-CT analysis showed that the newly formed bone in the BMP2-inc. BpNcCaP/HA-func. 3D scaffolds bore better quality and more mature microstructures than that in the group of 3D scaffold. In the group of BMP2-inc. BpNcCaP/HA-func. 3D scaffolds, the BVs in all the three 1/3 were significantly enhanced, which indicated that osteoinductivity overrided the osteoconduction and conferred a more homogenous bone distribution within the scaffolds. A similar bone distribution pattern was also found in the buccolingual direction in all the groups. The BVs in the coronal and middle 1/3 s were similar to each other, which indicated that the BMP2-inc. BpNcCaP/HA gel facilitated a significant vertical augmentation. Furthermore, histomorphometric analysis indicated the good osteointegration of the BMP2-inc. BpNcCaP/HA-func. 3D scaffolds with newly formed bone tissue.

One limitation in the present study was that only one type of scaffolds were adopted. Further studies may focus on the optimization of mechanical strength of and osteogenic properties within the scaffolds by modulating the pore size and struts thickness. Another limitation can be the short monitoring span, which excluded the possibility of collecting more data on scaffold degradation, bone remodeling and later implantation. Furthermore, more large animal studies should also be performed before extrapolating the present data to clinical application.

5 | Conclusion

In this study, we synthesized novel functionalized scaffolds with BMP-2/BpNcCaP/ HA-func. 3D scaffolds with an aim to develop properly mechanically-stable and highly osteoinductively-functionalized scaffolds to repair large vertical bone defects. The In vitro and In vivo data suggested a promising application potential of the functionalized scaffolds in repairing large vertical bone defects in dental clinic.

Author Contributions

Ting Wang involved in manuscript writing, animal experiment, data analysis and design; Gaoli Xu performed manuscript writing and data presentation; Chuankai Zhang carried out animal experiment and histological staining analyses; Tymour Forouzanfar involved in manuscript draft and final approval; Junwei Liang carried out animal experiment and data collection; Yulei Pan carried out animal experiment; Chenxi Shen performed histological staining analyses; Gang Wu performed project design, manuscript writing and final approval; Haiyan Lin carried out project support, critical review and final approval. All authors were involved in the paper writing and revising.

Acknowledgments

The authors thank laboratory technicians from the Research Base of Zhejiang Chinese Medical University, Hangzhou Stomatology Hospital, for their valuable help during the animal research.

Conflicts of Interest

The authors declare no conflicts of interest.

Data Availability Statement

The data pertaining to this study would be provided upon reasonable request from the first or corresponding author.

References

1. Y. Liu, G. Wu, and K. de Groot, "Biomimetic Coatings for Bone Tissue Engineering of Critical-Sized Defects," *Journal of the Royal Society Interface* 7, no. S5 (2010): S631–S647.

2. P. Galindo-Moreno, J. G. de Buitrago, M. Padial-Molina, J. E. Fernández-Barbero, J. Ata-Ali, and F. O'Valle, "Histopathological Comparison of Healing After Maxillary Sinus Augmentation Using Xenograft Mixed With Autogenous Bone Versus Allograft Mixed With Autogenous Bone," *Clinical Oral Implants Research* 29, no. 2 (2018): 192–201.

3. F. Migliorini, G. La Padula, E. Torsiello, F. Spiezia, F. Oliva, and N. Maffulli, "Strategies for Large Bone Defect Reconstruction After Trauma, Infections or Tumour Excision: A Comprehensive Review of the Literature," *European Journal of Medical Research* 26, no. 1 (2021): 118.

4. M. Chiapasco, E. Romeo, P. Casentini, and L. Rimondini, "Alveolar Distraction Osteogenesis vs. Vertical Guided Bone Regeneration for the Correction of Vertically Deficient Edentulous Ridges: A 1–3-Year Prospective Study on Humans," *Clinical Oral Implants Research* 15 (2004): 82–95.

5. S. H. Yu and H. L. Wang, "An Updated Decision Tree for Horizontal Ridge Augmentation: A Narrative Review," *International Journal of Periodontics and Restorative Dentistry* 42, no. 3 (2022): 341–349.

6. J. G. Christensen, G. P. Grønlund, S. R. Georgi, T. Starch-Jensen, N. H. Bruun, and S. S. Jensen, "Horizontal Alveolar Ridge Augmentation With Xenogenic Block Grafts Compared With Autogenous Bone Block Grafts for Implant-Retained Rehabilitation: A Systematic Review and Meta-Analysis," *Journal of Oral & Maxillofacial Research* 14, no. 2 (2023): e1.

7. C. M. Misch, H. Basma, M. A. Misch-Haring, and H. L. Wang, "An Updated Decision Tree for Vertical Bone Augmentation," *International Journal of Periodontics and Restorative Dentistry* 41, no. 1 (2021): 11–21.

8. I. A. Urban and A. Monje, "Guided Bone Regeneration in Alveolar Bone Reconstruction," *Oral and Maxillofacial Surgery Clinics of North America* 31, no. 2 (2019): 331–338.

9. T. Mikoya, N. Inoue, Y. Matsuzawa, Y. Totsuka, T. S. Kajii, and T. Hirosawa, "Monocortical Mandibular Bone Grafting for Reconstruction of Alveolar Cleft," *Cleft Palate-Craniofacial Journal* 47, no. 5 (2010): 454–468.

10. K. Sawada, K. Nakahara, M. Haga-Tsujimura, et al., "Comparison of Three Block Bone Substitutes for Bone Regeneration: Long-Term Observation in the Beagle Dog," *Odontology* 106, no. 4 (2018): 398–407.

11. P. Baldwin, D. J. Li, D. A. Auston, H. S. Mir, R. S. Yoon, and K. J. Koval, "Autograft, Allograft, and Bone Graft Substitutes: Clinical Evidence and Indications for Use in the Setting of Orthopaedic Trauma Surgery," *Journal of Orthopaedic Trauma* 33, no. 4 (2019): 203–213.

12. H. S. Sohn and J. K. Oh, "Review of Bone Graft and Bone Substitutes With an Emphasis on Fracture Surgeries," *Biomaterials Research* 23 (2019): 9.

13. R. Trombetta, J. A. Inzana, E. M. Schwarz, S. L. Kates, and H. A. Awad, "3D Printing of Calcium Phosphate Ceramics for Bone Tissue Engineering and Drug Delivery," *Annals of Biomedical Engineering* 45, no. 1 (2017): 23–44.

14. J. Wang, J. Guo, J. Liu, L. Wei, and G. Wu, "BMP-Functionalised Coatings to Promote Osteogenesis for Orthopaedic Implants," *International Journal of Molecular Sciences* 15, no. 6 (2014): 10150–10168.

15. W. H. K. Lo, B. D. Ulery, M. Deng, K. M. Ashe, and C. T. Laurencin, "Current Patents on Osteoinductive Molecules for Bone Tissue Engineering," *Recent Patents on Biomedical Engineering* 4, no. 3 (2011): 153–167.

16. A. W. James, G. LaChaud, J. Shen, et al., "A Review of the Clinical Side Effects of Bone Morphogenetic Protein-2," *Tissue Engineering Part B Reviews* 22, no. 4 (2016): 284–297.

17. G. Xu, C. Shen, H. Lin, et al., "Development, In Vitro Characterization and In Vivo Osteoinductive Efficacy of a Novel Biomimetically-Precipitated Nanocrystalline Calcium Phosphate With Internally-Incorporated Bone Morphogenetic Protein-2," *Frontiers in Bioengineering and Biotechnology* 10 (2022): 920696.

18. J. P. Schmitz and J. O. Hollinger, "The Critical Size Defect as an Experimental Model for Craniomandibulofacial Nonunions," *Clinical Orthopaedics and Related Research* 205, no. 205 (1986): 299–308.

19. G. M. Cooper, M. P. Mooney, A. K. Gosain, P. G. Campbell, J. E. Losee, and J. Huard, "Testing the Critical Size in Calvarial Bone Defects: Revisiting the Concept of a Critical-Size Defect," *Plastic and Reconstructive Surgery* 125, no. 6 (2010): 1685–1692.

20. S. K. Anwar and H. M. A. Hamid, "Immuno Histopathologic Evaluation of Mineralized Plasmatic Matrix in the Management of Horizontal Ridge Defects in a Canine Model (a Split Mouth Comparative Study)," *Odontology* 110, no. 3 (2022): 523–534.

21. H. F. Marei and K. Mahmood, "Critical Size Defects for Bone Regeneration Experiments in the Dog Mandible: A Systematic Review," *Implant Dentistry* 27, no. 1 (2018): 135–141.

22. S. Shanbhag, N. Pandis, K. Mustafa, J. R. Nyengaard, and A. Stavropoulos, "Alveolar Bone Tissue Engineering in Critical-Size Defects of Experimental Animal Models: A Systematic Review and Meta-Analysis," *Journal of Tissue Engineering and Regenerative Medicine* 11, no. 10 (2017): 2935–2949.

23. P. Su, L. Hyo-Jung, K. Keun-Suh, et al., "In Vivo Evaluation of 3D-Printed Polycaprolactone Scaffold Implantation Combined With β-TCP Powder for Alveolar Bone Augmentation in a Beagle Defect Model," *Materials* 11, no. 2 (2018): 238.

24. Z. G. Ma, K. Guo, L. Chen, X. Chen, D. Zou, and C. Yang, "Role of Periosteum in Alveolar Bone Regeneration Comparing With Collagen Membrane in a Buccal Dehiscence Model of Dogs," *Scientific Reports* 13 (2023): 2505.

25. F. Teng, L. Wei, D. Yu, et al., "Vertical Bone Augmentation With Simultaneous Implantation Using Deproteinized Bovine Bone Block Functionalized With a Slow Delivery of BMP-2," *Clinical Oral Implants Research* 31 (2020): 215–228.

26. M. Haga-Tsujimura, K. Nakahara, E. Kobayashi, K. Igarashi, B. Schaller, and N. Saulacic, "Single-Staged Implant Placement Using Bone Ring Technique With and Without Membrane Placement: An Experimental Study in the Beagle Dog," *Clinical Oral Implants Research* 29, no. 3 (2018): 263–276.

27. D. Rothamel, F. Schwarz, M. Herten, D. Ferrari, J. B. Oral, and M. Implants, "Vertical Ridge Augmentation Using Xenogenous Bone Blocks: A Histomorphometric Study in Dogs," *International Journal of Oral & Maxillofacial Implants* 24, no. 2 (2009): 243.

28. H. F. Marei, K. Mahmood, and K. Almas, "Critical Size Defects for Bone Regeneration Experiments in the Dog Mandible," *Implant Dentistry* 27, no. 1 (2018): 135–141.

29. R. K. Schenk, "Preparation of Calcified Tissues for Light Microscopy," *Methods of Calcified Tissue Preparation* 1 (1984): 1–56.

30. H. J. G. Gundersen and E. J. Jensen, "The Efficiency of Systematic Sampling in Stereology and Its Prediction," *Journal of Microscopy* 147, no. 3 (1987): 229–263.

31. A. R. Amini, C. T. Laurencin, and S. P. Nukavarapu, "Bone Tissue Engineering: Recent Advances and Challenges," *Biomedical Engineering* 40, no. 5 (2012): 363–408.

32. S. S. Lee, X. Du, I. Kim, and S. J. Ferguson, "Scaffolds for Bone-Tissue Engineering," *Matter* 5, no. 9 (2022): 2722–2759.

33. A. Sakkas, F. Wilde, M. Heufelder, K. Winter, and A. J. Schramm, "Autogenous Bone Grafts in Oral Implantology—Is It Still a "Gold Standard"? A Consecutive Review of 279 Patients With 456 Clinical Procedures," *International Journal of Implant Dentistry* 3 (2017): 1–17.

34. R. R. Betz, "Limitations of Autograft and Allograft: New Synthetic Solutions," *Orthopedics* 25, no. 5 (2002): S561–S570.

35. K.-m. Kim, S.-y. Choi, J.-H. Park, et al., "Six-Month Stability Following Extensive Alveolar Bone Augmentation by Sausage Technique," *Maxillofacial Plastic and Reconstructive Surgery* 45, no. 1 (2023): 16.

36. G. Fernandes, M. Aras, V. Chitre, A. Mysore, and S. Kamat, "Esthetic Rehabilitation of Partially Edentulous Ridge With Horizontal Bone Augmentation Using the Sausage Technique: A Report of Two Cases," *Cureus* 16 (2024): 3.

37. R. Ma, Q. Liu, L. Zhou, and L. Wang, "High Porosity 3D Printed Titanium Mesh Allows Better Bone Regeneration," *BMC Oral Health* 23, no. 1 (2023): 6.

38. H. Sopha, A. Kashimbetova, L. Hromadko, et al., "Anodic TiO2 Nanotubes on 3D-Printed Titanium Meshes for Photocatalytic Applications," *Nano Letters* 21, no. 20 (2021): 8701–8706.

39. F. Briguglio, D. Falcomatà, S. Marconcini, L. Fiorillo, R. Briguglio, and D. Farronato, "The Use of Titanium Mesh in Guided Bone Regeneration: A Systematic Review," *International Journal of Dentistry* 2019 (2019): 1–8.

40. H. Li, W. Fan, and X. J. Zhu, "Three-Dimensional Printing: The Potential Technology Widely Used in Medical Fields," *Journal of Biomedical Materials Research* 108, no. 11 (2020): 2217–2229.

41. C. Ghayor, I. Bhattacharya, and F. E. Weber, "The Optimal Microarchitecture of 3D-Printed β-TCP Bone Substitutes for Vertical Bone Augmentation Differs From That for Osteoconduction," *Materials & Design* 204 (2021): 109650.

42. T. S. Carvalho, P. M. Torres, J. H. Belo, J. Mano, and S. M. Olhero, "Bioactive Magnetic Materials in Bone Tissue Engineering: A Review of Recent Findings in CaP-Based Particles and 3D-Printed Scaffolds," *Advanced NanoBiomed Research* 3, no. 9 (2023): 2300035.

43. J. B. Vella, R. P. Trombetta, M. D. Hoffman, J. Inzana, H. Awad, and D. S. Benoit, "Three Dimensional Printed Calcium Phosphate and Poly(Caprolactone) Composites With Improved Mechanical Properties and Preserved Microstructure," *Journal of Biomedical Materials Research Part A* 106, no. 3 (2018): 663–672.

44. M. A. A. Ansari, A. A. Golebiowska, M. Dash, et al., "Engineering Biomaterials to 3D-Print Scaffolds for Bone Regeneration: Practical and Theoretical Consideration," *Biomaterials Science* 10, no. 11 (2022): 2789–2816.

45. D. Mumcuoglu, C. Siverino, B. Tabisz, B. Kluijtmans, and J. J. Nickel, "How to Use BMP-2 for Clinical Applications? A Review on Pros and Cons of Existing Delivery Strategies," *Journal of Translational Science* 3, no. 5 (2017): 1–11.

46. M. Hajimiri, S. Shahverdi, G. Kamalinia, and R. J. Dinarvand, "Growth Factor Conjugation: Strategies and Applications," *Journal of Biomedical Materials Research Part A* 103, no. 2 (2015): 819–838.

47. S. Cascone and G. J. Lamberti, "Hydrogel-Based Commercial Products for Biomedical Applications: A Review," *International Journal of Pharmaceutics* 573 (2020): 118803.

48. H. Huang, J. Feng, D. Wismeijer, G. Wu, and E. B. Hunziker, "Hyaluronic Acid Promotes the Osteogenesis of BMP-2 in an Absorbable Collagen Sponge," *Polymers* 9, no. 8 (2017): 339.

49. S. Cai, C. Wu, W. Yang, W. Liang, H. Yu, and L. Liu, "Recent Advance in Surface Modification for Regulating Cell Adhesion and Behaviors," *Nanotechnology Reviews* 9, no. 1 (2020): 971–989.

50. H. Amani, H. Arzaghi, M. Bayandori, et al., "Controlling Cell Behavior Through the Design of Biomaterial Surfaces: A Focus on Surface Modification Techniques," *Advanced Materials Interfaces* 6, no. 13 (2019): 1900572.

51. B. Majhy, P. Priyadarshini, and A. Sen, "Effect of Surface Energy and Roughness on Cell Adhesion and Growth – Facile Surface Modification for Enhanced Cell Culture," *RSC Advances* 11, no. 25 (2021): 15467–15476.

52. P. R. Buenzli, M. Lanaro, C. S. Wong, et al., "Cell Proliferation and Migration Explain Pore Bridging Dynamics in 3D Printed Scaffolds of Different Pore Size," *Acta Biomaterialia* 114 (2020): 285–295.

53. T. Fischer, A. Hayn, and C. T. J. S. Mierke, "Fast and Reliable Advanced Two-Step Pore-Size Analysis of Biomimetic 3D Extracellular Matrix Scaffolds," *Scientific Reports* 9, no. 1 (2019): 8352.

54. Y. Kuboki, Q. Jin, and H. Takita, "Geometry of Carriers Controlling Phenotypic Expression in BMP-Induced Osteogenesis and Chondrogenesis," *Journal of Bone and Joint Surgery* 83, no. 1 (2001): S105–S115.

55. E. Tsuruga, H. Takita, H. Itoh, Y. Wakisaka, and Y. Kuboki, "Pore Size of Porous Hydroxyapatite as the Cell-Substratum Controls BMP-Induced Osteogenesi," *Journal of Biochemistry* 121, no. 2 (1997): 317–324.

56. V. Karageorgiou and D. Kaplan, "Porosity of 3D Biomaterial Scaffolds and Osteogenesis," *Biomaterials* 26, no. 27 (2005): 5474–5491.

57. C. Ghayor and F. E. Weber, "Osteoconductive Microarchitecture of Bone Substitutes for Bone Regeneration Revisited," *Frontiers in Physiology* 9 (2018): 388969.

58. B. Al-Nawas and E. Schiegnitz, "Augmentation Procedures Using Bone Substitute Materials or Autogenous Bone-a Systematic Review and Meta-Analysis," *European Journal of Oral Implantology* 7, no. S2 (2014): S219–S234.

59. Y. Kuboki, H. Takita, D. Kobayashi, et al., "BMP-Induced Osteogenesis on the Surface of Hydroxyapatite With Geometrically Feasible and Nonfeasible Structures: Topology of Osteogenesis," *Journal of Biomedical Materials Research* 39, no. 2 (1998): 190–199.

60. S. J. Park, M. M. Rahman, J. Lee, S. W. Kang, and S. Kim, "Investigation of Bone Regeneration Efficacy of New Bovine Bone Minerals in a Canine Mandibular Critical Defect Model," *Advanced Healthcare Materials* 12, no. 22 (2023): 2202942.

61. J. S. Lee, J. S. Jung, G. I. Im, B. S. Kim, K. S. Cho, and C. S. Kim, "Ridge Regeneration of Damaged Extraction Sockets Using rhBMP-2: An Experimental Study in Canine," *Journal of Clinical Periodontology* 42, no. 7 (2015): 678–687.

62. J. P. Carrel, A. Wiskott, S. Scherrer, and S. Durual, "Large Bone Vertical Augmentation Using a Three-Dimensional Printed TCP/HA Bone Graft: A Pilot Study in Dog Mandible," *Clinical Implant Dentistry And Related Research* 18 (2016): 1183–1192.

63. J. G. Baldwin, F. Wagner, L. C. Martine, et al., "Periosteum Tissue Engineering in an Orthotopic in Vivo Platform," *Biomaterials* 121 (2017): 193–204.

64. S. Tamura, M. Mukaide, Y. Katsuragi, W. Fujii, K. Odaira, and N. J. T. Suzuki, "Periosteum-Derived Podoplanin-Expressing Stromal Cells Regulate Nascent Vascularization During Epiphyseal Marrow Development," *Journal of Biological Chemistry* 5 (2022): 298.

Supporting Information

Additional supporting information can be found online in the Supporting Information section.